Review Article

Thorsten Kramer*, Stefan Remund, Beat Jäggi, Marc Schmid and Beat Neuenschwander

Ablation dynamics – from absorption to heat accumulation/ultra-fast laser matter interaction

https://doi.org/10.1515/aot-2018-0010
Received January 26, 2018; accepted March 19, 2018

Abstract: Ultra-short laser radiation is used in manifold industrial applications today. Although state-of-the-art laser sources are providing an average power of 10–100 W with repetition rates of up to several megahertz, most applications do not benefit from it. On the one hand, the processing speed is limited to some hundred millimeters per second by the dynamics of mechanical axes or galvanometric scanners. On the other hand, high repetition rates require consideration of new physical effects such as heat accumulation and shielding that might reduce the process efficiency. For ablation processes, process efficiency can be expressed by the specific removal rate, ablated volume per time, and average power. The analysis of the specific removal rate for different laser parameters, like average power, repetition rate or pulse duration, and process parameters, like scanning speed or material, can be used to find the best operation point for microprocessing applications. Analytical models and molecular dynamics simulations based on the so-called two-temperature model reveal the causes for the appearance of limiting physical effects. The findings of models and simulations can be used to take advantage and optimize processing strategies.

Keywords: heat accumulation; laser ablation; microprocessing; shielding; ultra-fast laser.

PACS: 42.55.Px; 42.55.Rz; 42.55.Wd; 42.55.Xi; 42.60.-v; 42.62.-b; 42.62.Cf; 42.62.Fi; 52.38.Mf; 52.38.-r; 52.50.Jm; 79.20.Eb.

Communicated by: Thorsten Kramer

***Corresponding author: Thorsten Kramer,** Bern University of Applied Sciences BFH, Pestalozzistrasse 20, CH-3400 Burgdorf, Switzerland, e-mail: thorsten.kramer@bfh.ch
Stefan Remund, Beat Jäggi, Marc Schmid and Beat Neuenschwander: Bern University of Applied Sciences BFH, Pestalozzistrasse 20, CH-3400 Burgdorf, Switzerland

www.degruyter.com/aot

1 Introduction

The laser has come a long way since its invention in 1960, and its developer Theodore H. Maiman then called it, 'A Solution Seeking a Problem' [1]. At the beginning, the impact of the laser may have been bigger culturally than technologically; and only 4 years after, British Agent 007 was strapped to a table being menaced with one in the film, 'Goldfinger'.

However, in the same year, Hargrove et al. [2] report the first demonstration of an actively mode-locked laser, i.e. a helium-neon laser with an acousto-optic modulator. One year later, passive mode locking was demonstrated by Mocker and Collins [3], and this is the basis for a long-term stability of ultra-fast lasers. This was the beginning of the success story for ultra-fast lasers and laid the foundation for a myriad of innovative applications.

Within the next 20 years, ultra-fast laser systems mainly based on dyes were developed and improved, pulse duration was reduced from 10 ps to below 10 fs as shown in Figure 1, while at the same time, pulse energy and average power were increased to reach intensities of more than 10^{15} W/cm^2. This value could only further be raised after the development of chirped pulse amplification (CPA) by Strickland and Mourou [7].

Since the beginning of the 1990s solid state systems took over from dye systems due to their higher reliability and the possibility to reduce the size of the laser systems. Today, ultra-fast laser systems are able to deliver several hundreds of Watts average power und can work at frequencies up to the gigahertz range [4–6, 8–12].

Ultra-fast lasers have made their way from science labs to productions sides worldwide in manifold industrial applications ranging from automotive industries to medical technology, from mechanical engineering to pharmaceutical industries, and from watchmaking to aeronautic industries [13–20]. The technology was awarded with the 'Deutscher Zukunftspreis' in 2013 due to its paramount importance for, and crucial impact on, the German manufacturing industry and its global competitiveness (http://www.deutscher-zukunftspreis.de/de/news/deutscher-zukunftspreis-2013-festliche-preisverleihung-berlin).

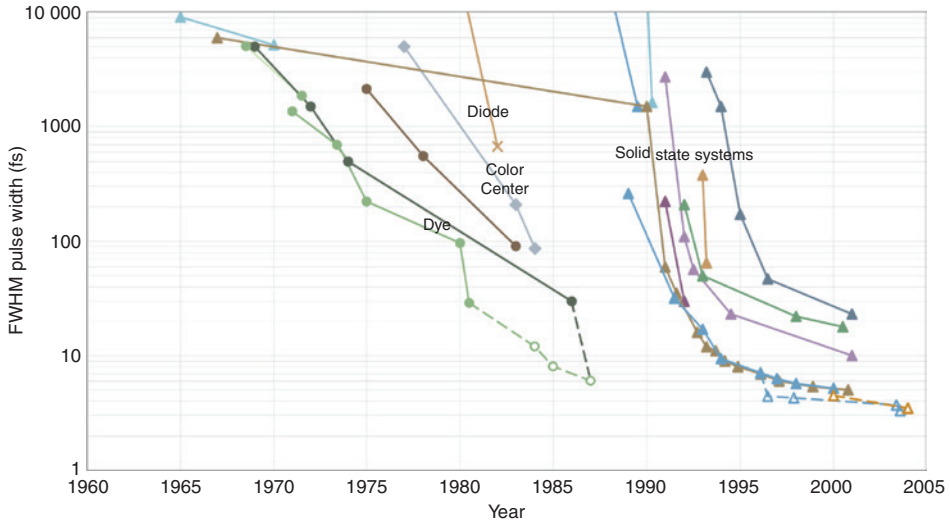

Figure 1: History of ultra-fast pulse duration, modified from Refs. [4–6].

2 Ablation process

2.1 Model

Ultra-short pulsed laser systems typically provide an excellent beam quality with $M^2 < 1.3$, which equates a Gaussian beam profile, i.e. the intensity distribution $I(r)$ in the focal spot can be considered as Gaussian-shaped.

The ablation depth z_{abl} (Eq. (1)) is, besides the penetration depth δ and the threshold fluence ϕ_{th}, depending on the fluence $\phi(r)$ itself that is directly defined by the intensity distribution $I(r)$ [13–16],

$$z_{abl} = \delta \cdot \ln\left(\frac{\phi(r)}{\phi_{thres}}\right) \tag{1}$$

Penetration depth δ and threshold fluence ϕ_{th} are material dependent and, for the sake of simplicity, will be considered as constant with respect to temperature changes. The intensity distribution $I(r)$, therefore, mainly defines the quantity of ablated material per pulse, i.e. the ablated volume per pulse. To demonstrate the difference in ablated volume per pulse, a Gaussian intensity distribution will be compared to a TopHat intensity distribution as shown in Figure 2.

In case of a TopHat distribution, the ablation depth z_{abl} can be written as

$$z_{abl}(r) = \begin{cases} \delta \cdot \ln\left(\dfrac{\phi}{\phi_{thres}}\right) & r \le R \\ 0 & r > R \end{cases} \tag{2}$$

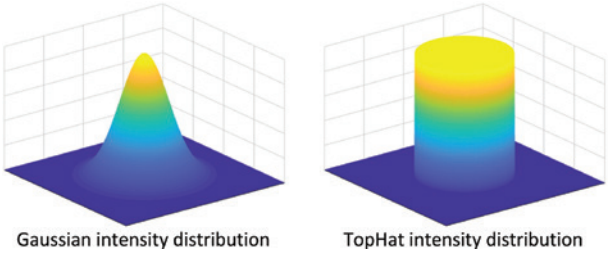

Figure 2: Intensity distributions.

and for a Gaussian intensity distribution as

$$z_{abl}(r) = \begin{cases} \delta \cdot \left(\ln\left(\dfrac{\phi_0}{\phi_{thres}}\right) - 2 \cdot \dfrac{r^2}{w_0^2}\right) & r \le R \\ 0 & r > R \end{cases} \tag{3}$$

with $R = w_0 \cdot \sqrt{\frac{1}{2} \cdot \ln\left(\frac{\phi_0}{\phi_{thres}}\right)}$ ablated radius and $\phi_0 = 2 \cdot \frac{E_H}{\pi w_0^2}$ peak fluence.

E_H is the pulse energy, and z_{abl} is the ablation depth for a Gaussian intensity distribution and is depicted in Figure 3.

$$\phi_0 = 2 \cdot \phi \tag{4}$$

Average fluence ϕ and peak fluence ϕ_0 are linked according to Eq. (4).

The ablated volume per pulse can be calculated and reads

$$\Delta V = \pi w_0^2 \cdot z_{abl} = \pi w_0^2 \cdot \delta \cdot \ln\left(\frac{\phi}{\phi_{thres}}\right) \tag{5}$$

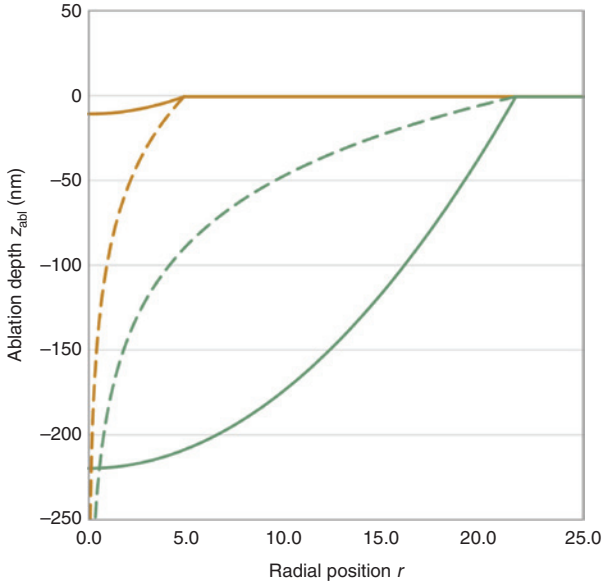

Figure 3: Ablation depth z_{abl} as a function of the radial position r or the deposited energy per volume dE/dV for a Gaussian intensity distribution for two different spot sizes (see Figure 5).

for a TopHat distribution and

$$\Delta V = \int_0^{2\pi}\int_0^{R} z_{\mathrm{abl}}(r)\cdot r\,dr\,d\varphi = \frac{\pi w_0^2}{4}\cdot\delta\cdot\ln^2\left(\frac{\phi_0}{\phi_{\mathrm{thres}}}\right) \tag{6}$$

for a Gaussian distribution. The ablated volume ΔV as a function of $\phi_0/\phi_{\mathrm{thres}}$ is shown in Figure 4.

Irrespective of the intensity distribution $I(r)$, in the case of pulsed laser radiation, the energy distribution or fluence $\phi(r)$ may directly be used to calculate the ablated volume per pulse.

In principle, the same steps must be followed for both intensity distributions, but the general approach is demonstrated for the TopHat only. The deposited energy per volume drops exponentially with the distance z from the surface [20]

$$\frac{dE}{dV}(z) = \frac{dE_0}{dV}\cdot e^{-\frac{z}{\delta}} \tag{7}$$

where $E_{\mathrm{tot}} = \frac{dE_0}{dV}\cdot\delta$ is the total absorbed energy and corresponds to the integral, i.e. the orange area under the curve in Figure 5.

The green area represents the amount of deposited energy that is required for the ablation process and amounts to

$$E_{\mathrm{abl}} = \frac{dE}{dV}(z_{\mathrm{abl}}) = \frac{dE_0}{dV}\cdot\frac{\phi_{\mathrm{thres}}}{\phi}\cdot\delta\cdot\ln\left(\frac{\phi}{\phi_{\mathrm{thres}}}\right) \tag{8}$$

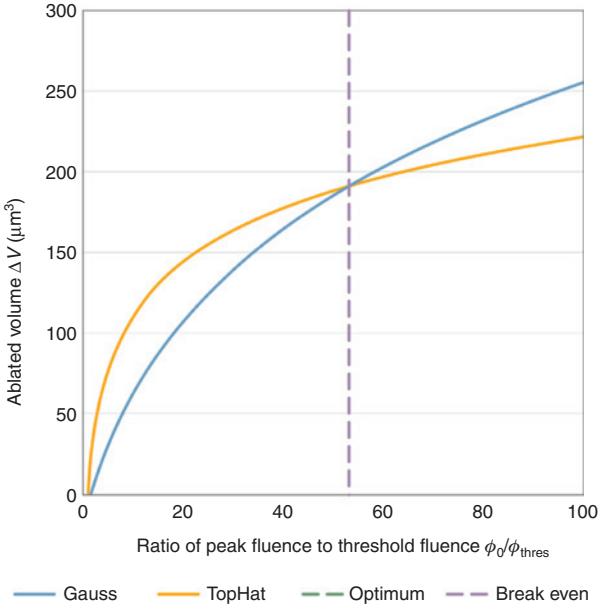

Figure 4: Ablated volume per pulse V_{abl} for a TopHat and a Gaussian intensity distribution and their ratio as a function of $\phi_0/\phi_{\mathrm{thres}}$ according to Eqs. (5) and (6). The optimum at $\phi_0 = e\cdot\phi_{\mathrm{thres}}$ and the break even at $\Delta V_{\mathrm{Gauss}}/\Delta V_{\mathrm{TopHat}} = 1$ are indicated. At the optimum, a TopHat is two times more efficient than a Gauss intensity distribution. The ablated volume has been calculated for a spot radius of $w_0 = 16$ µm and a penetration depth of $\delta = 0.06$ µm. Remark: An ablated volume of $\Delta V \approx 50$ µm³ corresponds to an ablation rate of $\Delta V/\Delta t \approx 8.3$ mm³/min at a repetition rate of $f_{\mathrm{rep}} = 2885$ kHz (see Figure 6).

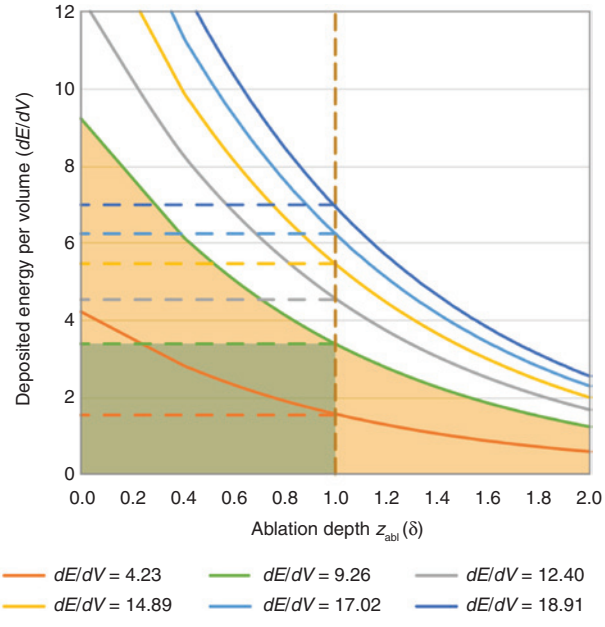

Figure 5: Deposited energy per volume dE/dV in dependence of the normalized depth z/δ. The orange area represents the total absorbed energy, whereas the green area represents the energy required for ablation.

By dividing the energy for the ablation process E_{abl} by the total absorbed energy E_{tot}, the process efficiency η can be defined as

$$\eta = \frac{\phi_{thres}}{\phi} \cdot \ln\left(\frac{\phi}{\phi_{thres}}\right) \tag{9}$$

and shows a maximum at $\phi = e\ \phi_{thres}$ with a maximum efficiency of $\eta = \frac{1}{e} = 0.368$. It is noteworthy that, in any cause, 63% of the applied energy is lost. The ablated depth then corresponds to the penetration depth $z_{abl} = \delta$.

The ablation rate $\Delta V/\Delta t$, i.e. the ablated volume per time, can be calculated by multiplying the ablated volume ΔV with the repetition rate f_{rep}

$$\frac{\Delta V}{\Delta t} = f_{rep} \Delta V \tag{10}$$

and the ablation rate can be written as

$$\frac{\Delta V}{\Delta t} = \pi w_0^2 \cdot \delta \cdot f_{rep} \cdot \ln\left(\frac{P_{ave}}{f_{rep} \cdot \pi w_0^2 \cdot \phi_{thres}}\right) \tag{11}$$

for a TopHat and

$$\frac{\Delta V}{\Delta t} = \frac{\pi w_0^2}{4} \cdot \delta \cdot f_{rep} \cdot \ln^2\left(\frac{2 \cdot P_{ave}}{f_{rep} \cdot \pi w_0^2 \cdot \phi_{thres}}\right) \tag{12}$$

for a Gaussian intensity distribution.

It has to be mentioned that both intensity distributions show a maximum. This maximum defines the highest ablation rate and can be referred to as optimum. In Figure 6, the repetition rate f_{rep} is increased, while the average power P_{ave} is kept constant. Therefore, the fluence reduces with increasing repetition rate and, in the case of the TopHat, falls below the threshold fluence. The optimum frequencies $f_{rep,opt}$, that are defined by the highest ablation rate $\Delta V/\Delta t_{max}$, are given by

$$f_{rep,opt} = \frac{P_{ave}}{e \cdot \pi w_0^2 \cdot \phi_{thres}} \tag{13}$$

for a TopHat and by

$$f_{rep,opt} = \frac{2 \cdot P_{ave}}{e^2 \cdot \pi w_0^2 \cdot \phi_{thres}} \tag{14}$$

for a Gaussian intensity distribution.

The optimum repetition rate $f_{rep,opt}$, on the one hand, scales linearly with the average power P_{ave}, which implies that the scanning speed needs to be increased by the same factor if the spatial pulse distance is kept.

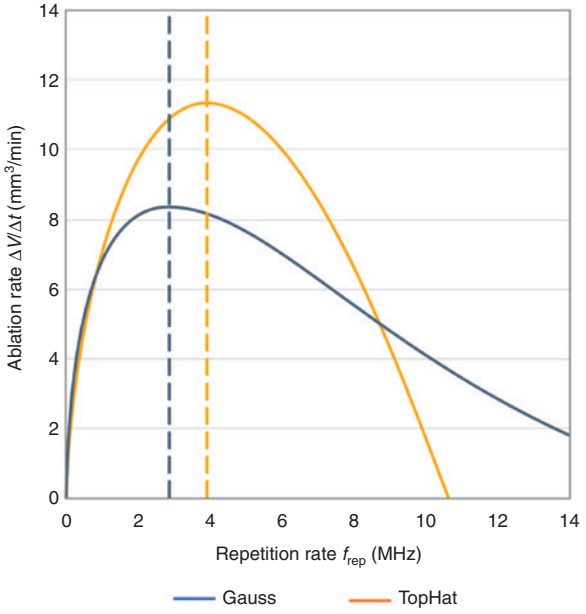

Figure 6: Ablation rate $\Delta V/\Delta t$ for a TopHat and a Gaussian intensity distribution as a function of the repetition rate f_{rep}. according to Eqs. (11) and (12). The optimum frequency for both intensity distributions can be calculated according to Eqs. (13) and (14). The following data was used: $P_{ave} = 30$ W, $w_0 = 16$ µm, $\phi_0 = 0.35$ J/cm², $\delta = 0.06$ µm.

On the other hand, the optimum repetition rate $f_{rep,opt}$ does scale reciprocal with the spot size πw_0^2. When the spot radius w_0 is reduced by a factor of two, the repetition rate f_{rep} must be increased by a factor of four.

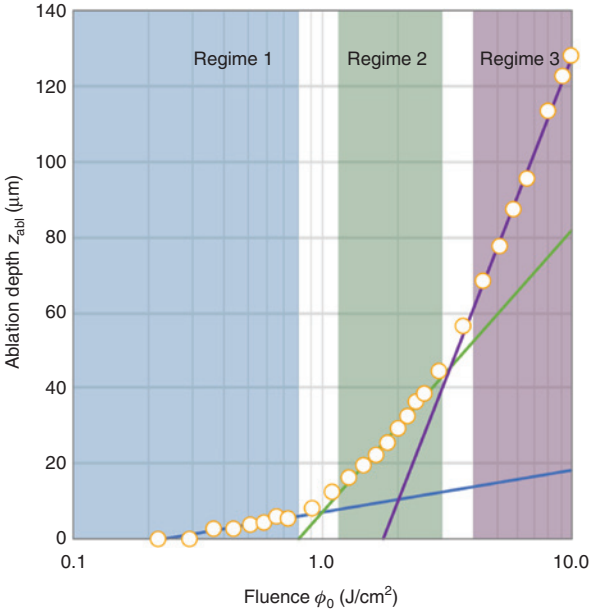

Figure 7: Ablation depth z_{abl} as a function of the laser peak fluence ϕ_0 for copper showing three ablation regimes [22–24]. Each regime can be described by an individual threshold fluence ϕ_{thres}.

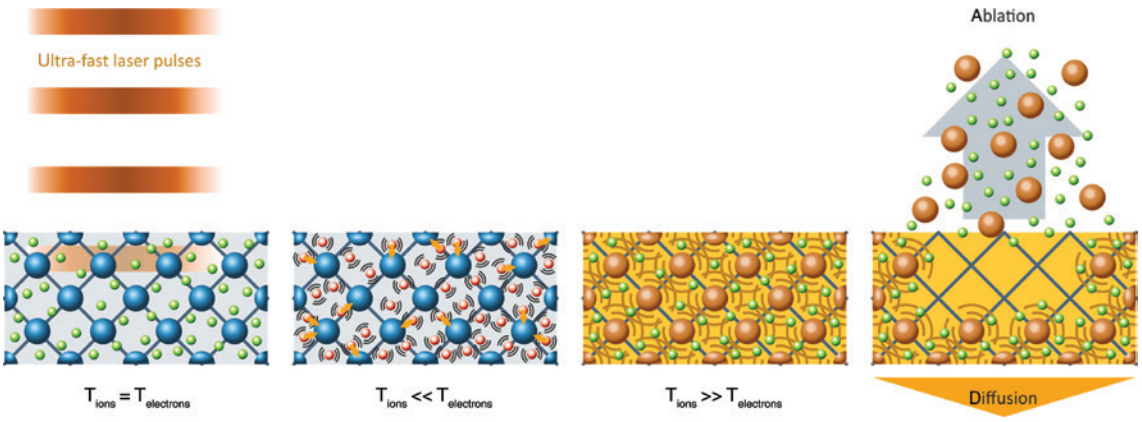

Figure 8: Two-temperature model for ultra-fast laser ablation processes: basic mechanisms. The energy of the photons is absorbed by the electrons and then transferred to the lattice by collisions. On the short timescale, the temperatures of the electrons and the lattice is different (modified from Ref. [25]).

When increasing the fluence, different ablation mechanisms become dominant [21–23]. Macroscopically these ablation mechanisms can be demonstrated by plotting the ablation depth z_{abl} against the natural logarithm of the peak fluence ϕ_0 as shown in Figure 7 [22, 23]. The ablation mechanisms are defining an ablation regime that is characterized by a linear increase in the ablation depth z_{abl} as a function of the natural logarithm of the peak fluence ϕ_0.

Threshold fluence ϕ_{thres} as well as penetration depth δ, in principal, are material and wavelength dependent, but in addition, they change with the ablation mechanism for each regime. Each ablation regime then can be described by an individual threshold fluence ϕ_{thres} and penetration depth δ.

The energy of the photons of the ultra-short laser pulses that are penetrating the bulk material is absorbed by free electrons in the skin layer of a metal. The energy drops exponentially with the depth as shown in Figure 5. The electrons are being accelerated, which is equivalent to a rise in the temperature of the electrons. They collide with ions in the lattice transferring their kinetic energy to the lattice. Because of their higher mass, the ions accelerate much slower representing a retarded, but still rapid, rise in the temperature of the lattice, whereas the temperature of the electrons drops much faster. Depending on the absorbed fluence and the pulse duration, the material is ablated by different ablation modes. The basic mechanisms are schematically depicted in Figure 8. The fundamental description of the temperature distributions is called the two-temperature model that distinguishes between the individual temperature of the electrons and the lattice that was introduced by Anisimov et al. [26, 27]. Figure 9 shows an example of a two-temperature Model

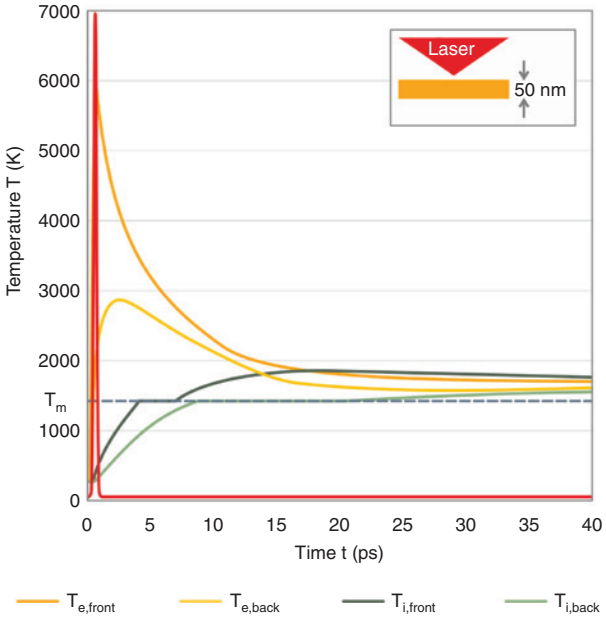

Figure 9: Two-temperature model: electron and lattice temperatures at both surfaces of a nickel film, irradiated with a 200-fs laser around melting threshold (absorbed fluence 43 mJ/cm^2) (modified from Refs. [28] and [29]).

simulating the irradiation of a 50-nm nickel foil with a 100-fs laser pulse [28, 29].

Theoretical predictions like melting thresholds or heating rates can be made by means of the two-temperature model, and it has widely been applied to explain the experimental results during ultra-short pulse material processing [30].

In Figure 9, the laser pulse as well as the temperature of the electrons (orange lines) and the temperature of the ions (green lines) on the front surface and on the back surface

are shown. The temperature of the electrons on the front surface rises immediately with the incident laser pulse. The increase in the temperature of the lattice is much slower, but after approximately 4 ps, the front surface starts to melt already, and after approximately 8 ps, the surface on the back reaches the melting temperature as well.

2.2 Ablation modes

During the past three decades, the understanding of the process for ultra-short/ultra-fast pulsed laser ablation substantially changed. In the early years of materials processing with ultra-short pulsed laser radiation, it was assumed that the high intensity of the ultra-short laser pulses was able to directly evaporate a material (sublimation). As the repetition rates of the ultra-short pulsed lasers was in the range of some 10 kHz, the term 'cold ablation' was used to describe the application of ultra-short pulsed lasers. Increasing the repetition rate and average power shed a different light on 'cold ablation', and heat accumulation stepped into the limelight of the researchers (see Section 2.3). In addition, the enormous rise in computing power helped to increase and deepen the understanding of ultra-fast ablation.

Nowadays, the ablation process is described in a more differentiated manner than by the mere calculation

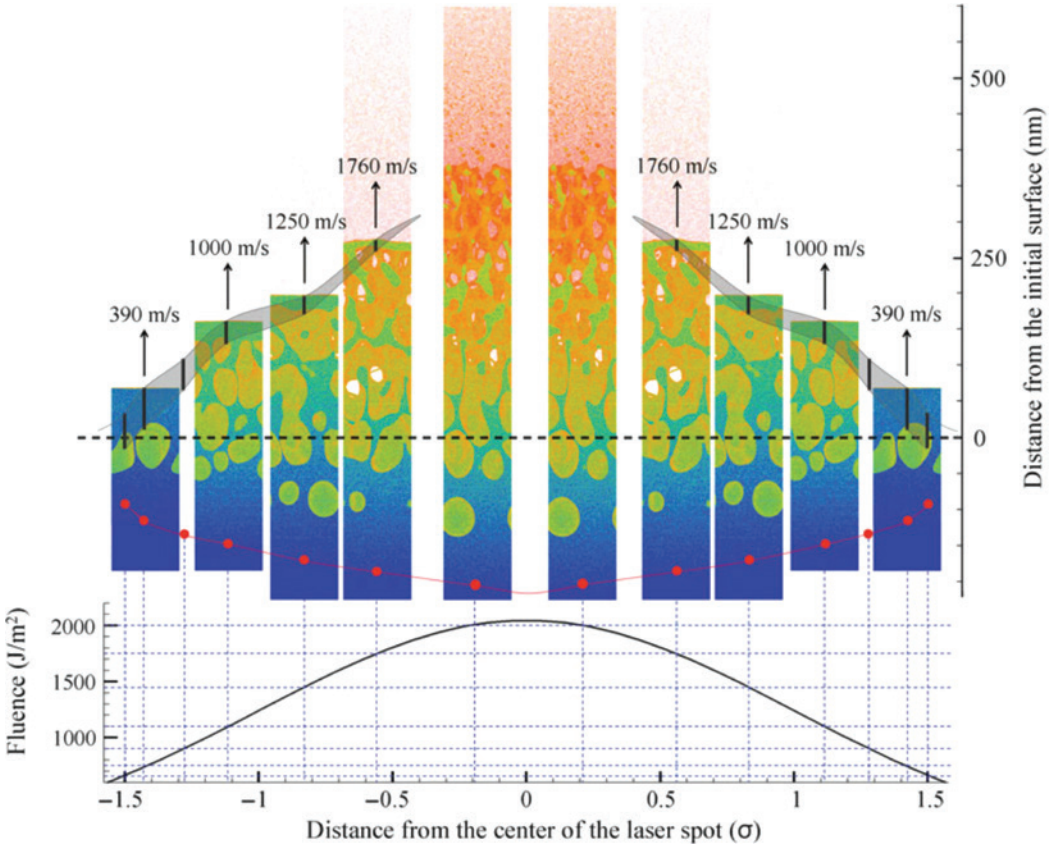

Figure 10: The integral visual picture of melting, generation of subsurface voids, and material ejection from an aluminum target irradiated by a 100-fs laser pulse. The laser beam has a Gaussian spatial profile with a peak absorbed laser fluence of 2050 J/m², as shown in the bottom part of the figure. The representation of the laser-induced processes at the scale of the whole laser spot is based on a 'mosaic approach', where snapshots from individual TTM-MD simulations taken at the same time of 150 ps after the laser pulse are aligned with locations within the laser spot that correspond to the values of local fluence used in the simulations, as shown by the thin vertical and horizontal dashed lines. The atoms in the snapshots are colored by their potential energy, from blue for low-energy atoms in the bulk of the target to *red* for the vapor-phase atoms. The red dots connected by the red line mark the location of the melting front. The thicknesses and locations of the top void-free layers are shown by black bars for simulations performed in the spallation regime and, in the case of the lowest fluence of 650 J/m², just below the spallation threshold. For two local fluences, 650 and 900 J/m², the locations of the melting front and the void-free layers are marked without showing the corresponding snapshots. The velocities of the top void-free layers at 150 ps are provided in the figure [31]. Reprinted by permission from: Springer Nature, Applied Physics A (January 2014) Volume 114, Issue 1, pp 11–32, Materials Science and Processing: "Microscopic mechanisms of laser spallation and ablation of metal targets from large-scale molecular dynamics simulations", Wu, C. and Zhigilei, L.V., doi.org/10.1007/s00339-013-8086-4.

of temperature fields. In particular, molecular dynamics (MD) simulations based on the two-temperature model have proven to be capable of delivering results for metals that provide information on the mechanisms of laser melting and resolidification [31–39], generation of crystal defects [40–42], photomechanical spallation [34, 37, 39, 43–50], phase explosion, and material ejection in laser ablation [33, 37, 39, 43, 48, 49, 51–71].

The energy deposition during an ultra-short laser pulse creates a so-called inertial stress confinement [37, 43, 45], which characterizes the inability of the material to expand during the time of ultra-fast heating by the laser pulse. As a consequence, strong compressive stresses are built up in the surface region. When these stresses relax, they cause the generation and growth of sub-surface voids which, in turn, may cause separation and ejection of liquid surface layers or droplets from the bulk.

Wu and Zhigilei [31] performed a series of TTM-MD simulations for femtosecond laser irradiation of Al and combined them to an impressing overview, a 'mosaic approach' or 'the big picture' as they call it. In Figure 10, it is reprinted by permission including the explanation in the caption.

They distinguish between two regimes, photomechanical spallation and phase explosion, and report an abrupt change in the composition of the ejected plume when the laser fluence increases above the spallation threshold. The ejection of liquid layers and large droplets give way to a mixture of atoms, atomic clusters, and small droplets. This phase explosion regime is caused by the overheating above the limit of thermodynamic stability of the liquid layer [31, 72], whereas the relaxation of the induced photomechanical stresses is the reason for the material ejection at lower fluences.

Photomechanical spallation or explosive decomposition of superheated material may lead to unusual metastable phases or complex surface morphologies. Especially for metals, high cooling rates of up to 10^{12} K/s caused by the local high energy concentration and the large thermal conductivity arise [72–74], and a highly undercooled liquid is generated. The formation of unusual defect configurations, nanocrystalline, and amorphous structures are possible effects [73–77].

2.3 Heat accumulation

For the description of the ablation modes, only a single pulse and a timescale of some tens of picoseconds have been considered. Applying a series of pulses requires a longer time base and the consideration of accumulation effects, e.g. heat accumulation or shielding gets important. Heat accumulation refers to the continuous increase in temperature of the target due to the fact that the time between two consecutive pulses is too short to allow the material to

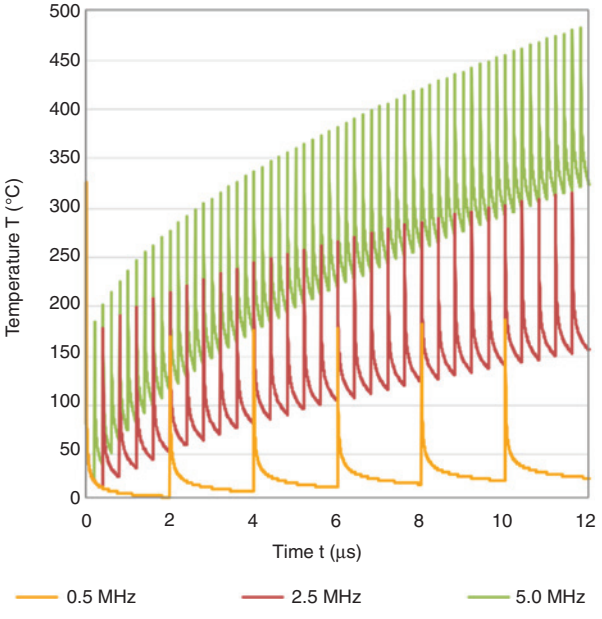

Figure 11: Example for heat accumulation due to the increase in the repetition rate: temperature on the surface as a function of time for three different repetition rates $f_{rep} = 0.5$ MHz, $f_{rep} = 2.5$ MHz and $f_{rep} = 5.0$ MHz on the surface of the target ($z = 0$) [78].

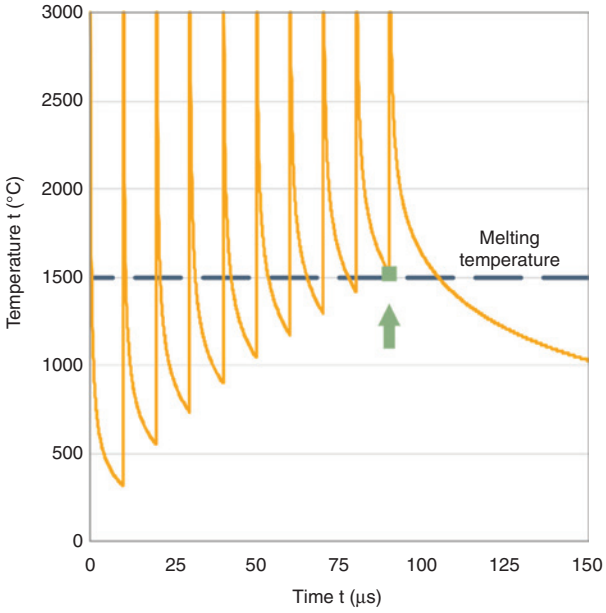

Figure 12: Heat accumulation in stainless steel AISI 304 at a high pulse energy $E_H = 3$ mJ and at a repetition rate of $f_{rep} = 100$ kHz. The tenth pulse hits a molten surface [80].

fully cool down. The remaining energy in the material is then referred to as residual heat. In this context, the influence of the high repetition rates of state-of-the-art ultra-fast laser systems must be investigated. Simple heat conduction calculations demonstrate that a surface irradiated by laser pulses at low repetition rates stays cool, whereas at high repetition rates, and keeping the same pulse energy, it heats up rapidly. Figure 11 shows examples for stainless steel AISI 304 at three repetitions rates [78–80].

Weber et al. [80] derived approximation formulas to calculate the residual heat, respectively, the heat accumulation, and the temporal evolution of the temperature of a stationary spot for one-dimensional to three-dimensional heat flow:

$$\Delta T_{nD}\left(t=\frac{N_i}{f_{\mathrm{rep}}}\right)=\frac{Q_{nD}}{\rho\cdot c_p\cdot\sqrt{\left(\frac{4\cdot\pi\cdot\kappa}{f_{\mathrm{rep}}}\right)^{nD}}}\cdot\sum_{N=1}^{N_i}\frac{1}{\sqrt{N^{nD}}} \tag{15}$$

where $\Delta T_{HA,nD}$ is the temperature increase, N_i is the number of heat inputs (consecutive laser pulses) at a given repetition rate f_{rep}, and nD denotes the dimensionality $nD \in \{1, 2, 3\}$. Figure 12 shows the calculation results for stainless steel and 10 consecutive pulses with a pulse energy of $E_{\mathrm{H}}=3$ mJ at a repetition rate of $f_{\mathrm{rep}}=100$ kHz according to Eq. (15). The 10th pulse already hits a molten surface, and the ablation process may change drastically, typically reducing the efficiency and quality.

Furthermore, they found that the maximum number of consecutive pulses per location decreases by P_{ave}^{-2} but increases linearly with the feed rate.

Bauer et al. [81] reported the influence of heat accumulation on the surface quality for the micromachining of stainless steel AISI 304 with picosecond laser radiation. They found a critical saturation temperature of approximately $T_{\mathrm{sat,crit}}=610°\mathrm{C}$, where the quality of the ablated surface drastically decreases; it changes from a smooth and reflective surface to a rough, bump covered surface. They developed an analytic model to predict the critical saturation temperature. Three-dimensional simulations of the temperature fields that consider the temporal and spatial displacement of the consecutive laser pulses are the basis for a heat flow model to describe heat accumulation for scanning ultra-short pulse laser machining [81].

2.4 Shielding

Besides heat accumulation that reduces the range of laser parameters, in particular, repetition rate f_{rep} and peak fluence ϕ_0, and process parameters like scanning speed v_{scan}, the subsequent laser pulse interacts with the ablated material of the previous one as well.

Koenig et al. [82] investigated the plasma evolution during laser ablation with ultra-short pulsed laser radiation. By means of pump-and-probe experiments, they measured the transmission of the plasma/particle plume for the ablation of aluminum as well as copper and steel targets and discovered two transmission minima at approximately $t_1=5$ ns and $t_2=150$ ns after the laser pulse independent of the target material. The extent of the transmission reduction differed for each material.

Figure 13 is reprinted by permission and shows the temporal transmission of aluminum as well as of copper and steel. The repetition rates corresponding to the time of the minima are $f_{\mathrm{rep}}(t_1=5\ \mathrm{ns})=200$ MHz and $f_{\mathrm{rep}}(t_2=150\ \mathrm{ns})=7$ MHz, respectively. In all cases, the transmission recovers to 100% after about $t_{\mathrm{rec}}=5$ µs after the laser pulse; this corresponds to a repetition rate of $f_{\mathrm{rep,rec}}=0.2$ MHz.

Although the peak fluences of $\phi_0=17$ J/cm² and $\phi_0=18$ J/cm², respectively, are far above the ones used for micromachining, typically around $\phi_0=0.5$ J/cm² for steel and $\phi_0=3$ J/cm² for copper, applications at repetition rates in the range of 0.2 MHz to 2 MHz may already suffer from an efficiency loss due to the reduced transmission of the incident ultra-fast laser radiation through the plume.

3 Industrial relevance

3.1 Quality and ablation process

From the point of view of the user, the previous findings become interesting if the quality of the results or the effectiveness of the process is affected. Then, there must be a strategy to either avoid or to exploit the above-mentioned effects with respect to the objective that must be optimized. Furthermore, the dependence of the objective on the individual laser and process parameters finally defines the stability and robustness of the process around the chosen operating point.

Knowledge of the behavior on a certain parameter over a larger range then can be used to upscale the ablation process, e.g. to higher repetition rates or higher average power.

3.2 Steel

A lot of investigations have been performed on stainless steel AISI 304 regarding heat accumulation and shielding

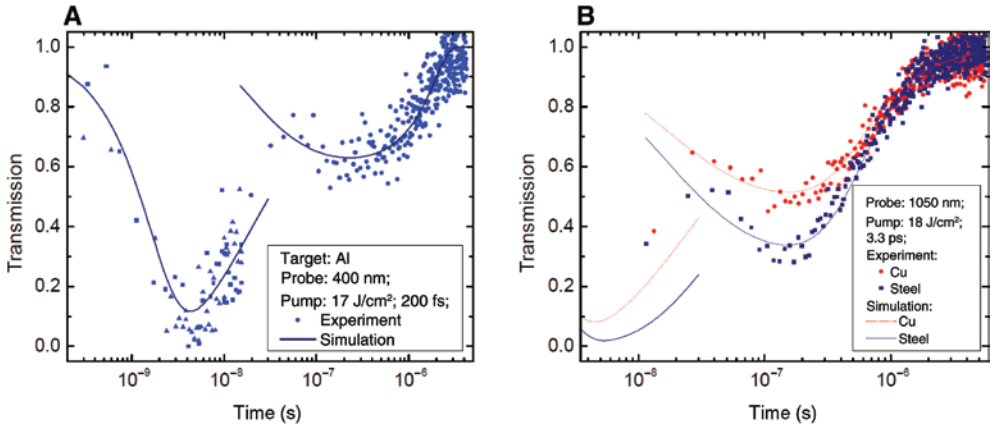

Figure 13: Temporal transition of probe pulses with a wavelength of $\lambda_{probe} = 400$ nm for the ablation al aluminum with $\tau_H = 200$ fs pulses at a peak fluence of $\phi_0 = 17$ J/cm² (A); temporal transmission of probe pulses with a wavelength of $\lambda_{probe} = 1050$ nm for ablation of $\tau_H = 3.3$ ps pulses at $\phi_0 = 18$ J/cm² (B) [82]. Reprinted by permission from: The Optical Society of America, Optics Express Vol. 13, Issue 26, pp. 10597–10607 (2005): "Plasma evolution during metal ablation with ultrashort laser pulses", J. König, S. Nolte, and A. Tünnermann, doi.org/10.1364/OPEX.13.010597.

effects. The results of the investigations on upscaling to higher repetition rates and higher power, therefore, can well be positioned in the context of these reported effects.

Jaeggi et al. [23] performed experiments on steel and copper with ultra-fast laser radiation at repetition rates up to 40 MHz and an average power of up to 365 W. Figure 14 shows the specific removal rate, the ablated volume per time, and average power $dV/(dt\ P_{ave})$, as a function of the peak fluence ϕ_0 for different repetition rates. The values for low repetition rates are produced with different lasers at different pulse durations and are added for the sake of completeness (see Section 3.4). The efficiency increases for repetition rates of 8.1 MHz and 10 MHz at 3.3 ps compared to 0.2 MHz at 10 ps but is still lower than for 0.5 MHz at 350 fs, and the maximum shifts slightly to a higher peak fluence. The optimum peak fluence is approximately 0.4–0.5 J/cm². At peak fluences exceeding 1 J/cm², the ablation at 10 MHz is more efficient than at 8.1 MHz. A further increase in the repetition rate to 40 MHz again brings the ablation efficiency back down to the level of 0.2 MHz but compresses the maximum and shifts it to a lower peak fluence. Peak fluences above 0.6 J/cm² could not be investigated due to the limit of the average power of 365 W.

Figure 15 shows three SEM images of the surfaces machined at different repetition rates and different average power. At the lowest repetition rate of 0.2 MHz and the lowest average power of 0.4 W, the surface is smooth and shiny, whereas for both higher repetition rates of 10 MHz and 40 MHz and average powers of 54 W and 155 W, respectively, the surface quality is rough and bumpy. This surface structure is comparable to the one presented by Bauer et al. when the surface temperature exceeded the critical saturation temperature and, therefore, is an aftermath of heat accumulation.

The impact of heat accumulation can be reduced if the number of pulses per location is reduced either by reducing the repetition rate (temporal measure) or by reducing the overlap (spatial measure).

Reducing the repetition rate while keeping the optimum peak fluence means to reduce the applied average power by the same factor, and probably, the user cannot take full advantage of the laser.

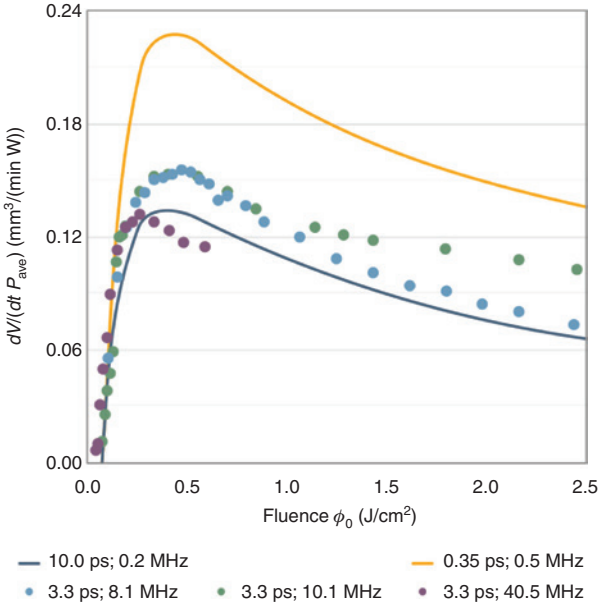

Figure 14: Specific removal rate for steel AISI 304 at different repetition rates [23].

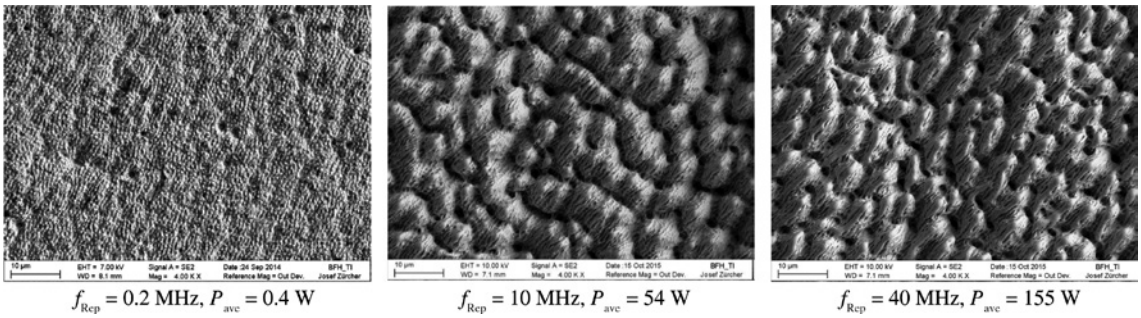

Figure 15: SEM images of machined surfaces in stainless steel AISI 304 at different repetition rates and different average power [23].

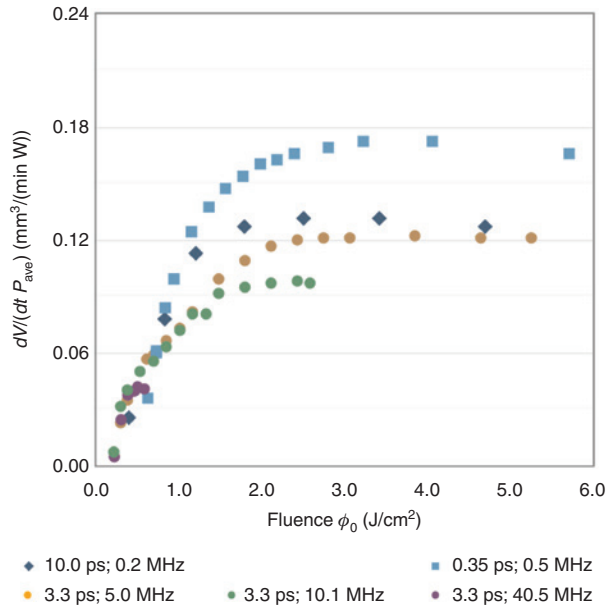

Figure 16: Ablation efficiency of copper (C12 200) at different repetition rates and overlaps [23].

Reducing the overlap, thus increasing the distance between successive pulses, means to increase the scanning speed. In this case, the scanning device becomes the limiting factor; glavanometric scanners may reach some tens of meters per second depending on the focusing optics, e.g. 40 m/s for f=163 mm [83]. In contrast, polygon scanners go up to several hundreds of meters per second but do not offer the same flexibility as galvanometric scanners.

As a consequence, novel machining strategies besides the improvement of the equipment and hardware have to be developed to fully benefit from state-of the-art ultrafast lasers for micromachining of metals. A few ideas will be presented in Section 3.5.

3.3 Copper

The specific removal rate for copper (C12 200) at different repetition rates is shown in Figure 16. The values for 0.5 MHz are taken from the results for a pulse duration of 350 fs. Compared to the results for steel, the ablation efficiency for copper, in general, is lower, and the optimum range is much broader. The optimum peak fluence is 2.5–4.0 J/cm². The ablation efficiency strongly drops with the increase in peak fluence. From 2 MHz to 10 MHz, it drops by 25% and from 10 MHz to 40 MHz by another 50%.

The maximum ablation rate was obtained at a repetition rate of f_{rep}=5 MHz and the maximum average power

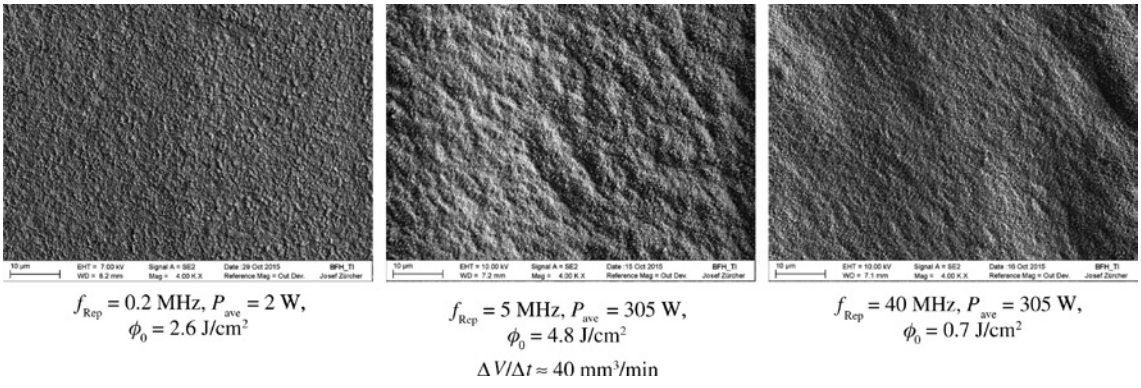

Figure 17: SEM images of machined surfaces in copper (C12 200) at different repetition rates and different average power [23].

of $P_{ave} = 306$ W and amounted to $\Delta V/\Delta t \approx 40$ mm³/min. The surface quality at this point is still high. Figure 17 shows SEM images of the surfaces machined at different repetition rates and a different average power.

A decrease in the surface quality to the extent as for steel could not be observed for copper as shown in Figure 17.

3.4 Pulse duration

The influence of the pulse duration has been the topic of several publications [22, 84–89]. For the multitude of materials, the motto 'the shorter, the better' applies when it comes to the choice of a femtosecond or a picosecond laser, although the differences for pulse duration below 1 ps are small.

Figures 18 and 19 show the specific removal rates of stainless steel AISI 304 and copper (C12 200). Both graphs prove that, in general, the shortest pulse duration investigated has the highest specific removal rate. The influence of the pulse duration on the specific removal rate is more pronounced for stainless steel than it is for copper.

3.5 Upscaling

As shown before, the upscaling of the experimental results obtained at a low average power and low repetition rates is not possible when effects like heat accumulation or shielding occur. To take advantage of the average power and repetition rates of state-of-the-art ultra-fast lasers, the appearance of these effects has to be avoided by either separation of the consecutive pulses spatially or temporally. Increasing the scanning speed for galvanometric scanners is limited by the hardware; changing to a polygon scanner increases the scanning speeds, and both limits the flexibility at the same time.

If the spot size is increased to keep the optimum peak fluence but a higher average power is applied, the minimum feature size will be increased to the same extent.

As an alternative, the number of spots can be increased. At present, the diffractive optical elements (DOEs) or spatial light modulators (SLMs) can be used to generate multiple spots of different shapes, matrices of 2×2, 3×3, etc., spots can be used to machine a large surface or to machine a higher number of pieces at the same time with the same structure [90]. SLMs are providing a higher flexibility, but they underlie some restrictions like destruction threshold, resolution, or switching frequency [91, 92].

Ultra-fast lasers in MOPA arrangement provide so-called pulse bursts, pulse trains of a defined number of consecutive pulses at the frequency of the seed oscillator. Pulse bursts can be used to increase the productivity of the laser; various investigations reveal that the ablation efficiency can be kept or even increased for several configurations of the pulse bursts [93–99].

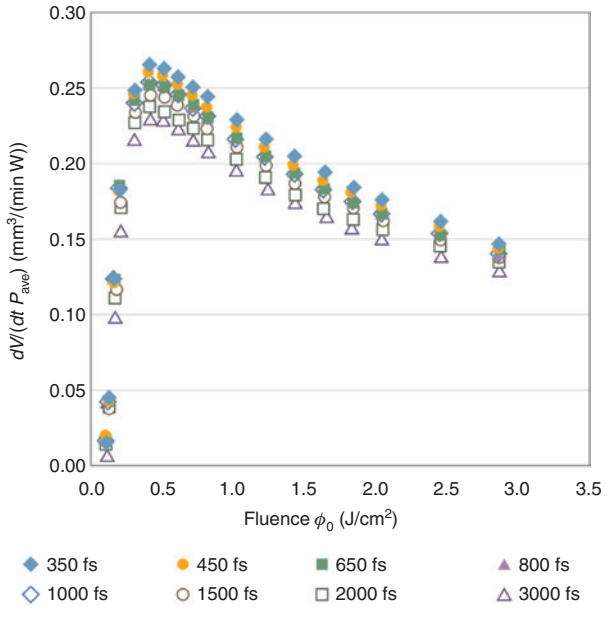

Figure 18: Influence of the pulse duration on the specific removal rate of stainless steel AISI 304 [22].

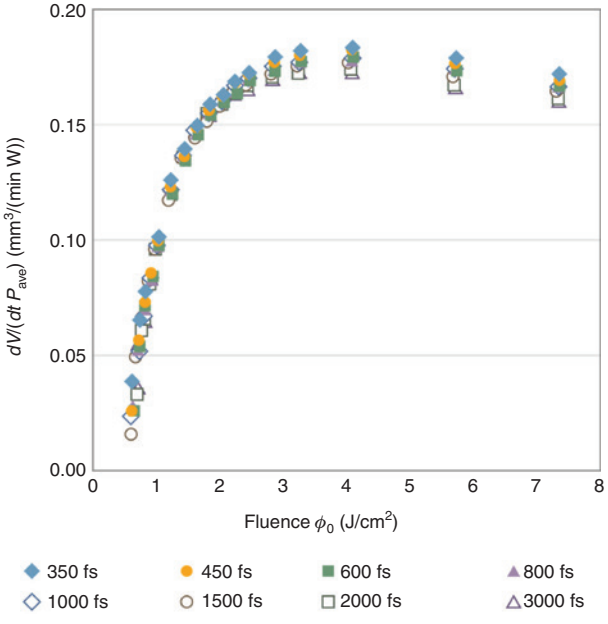

Figure 19: Influence of the pulse duration on the specific removal rate of copper (C12 200) [22].

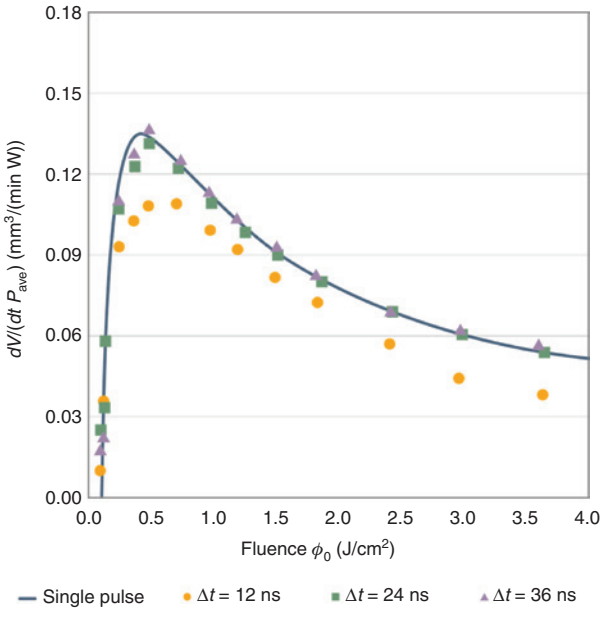

Figure 20: Specific removal rate for the application of a two-pulse burst on steel (AISI 304) [97, 98].

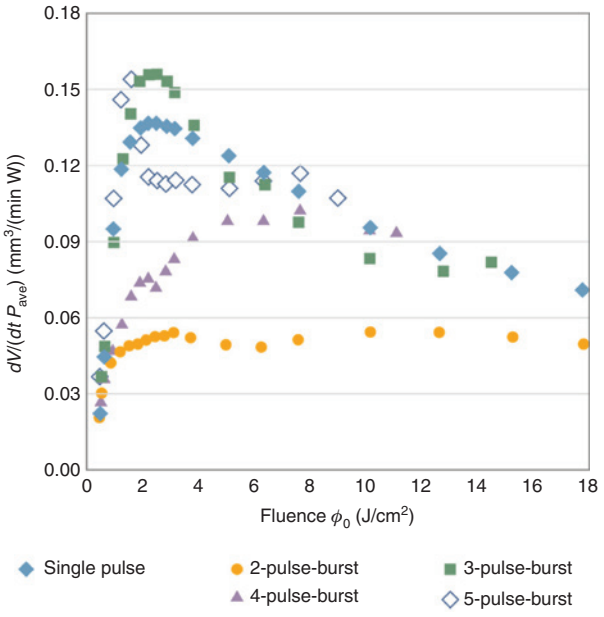

Figure 22: Specific removal rate for the application of pulse bursts on copper (C12 200) [97, 98, 100]. The pulse distance between two consecutive pulses for all bursts is 12 ns.

In Figures 20 and 21, the specific removal rate for stainless steel AISI 304 as a function of the peak fluence is shown for a two-pulse burst with varying inter-pulse-distances and a three-pulse burst, respectively. The highest removal rate is achieved with a single pulse, but a two-pulse burst with an inter-pulse distance of at least 24 ns ablates the same amount of material per time and average power, i.e. it has the same ablation efficiency per pulse. This means that each pulse of the two-pulse burst ablates as much material as a single pulse and a two-pulse burst, therefore, it ablates twice as much as a single pulse at the same repetition rate. The user can benefit from this by applying a two-pulse-burst

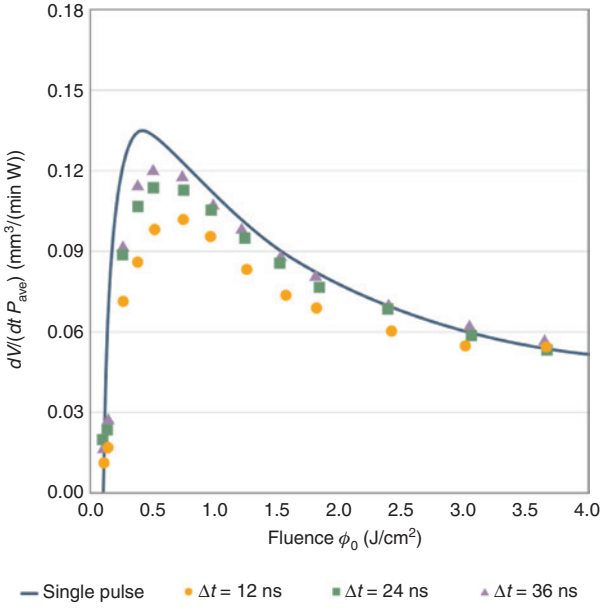

Figure 21: Specific removal rate for the application of a three-pulse burst on steel (AISI 304) [97, 98].

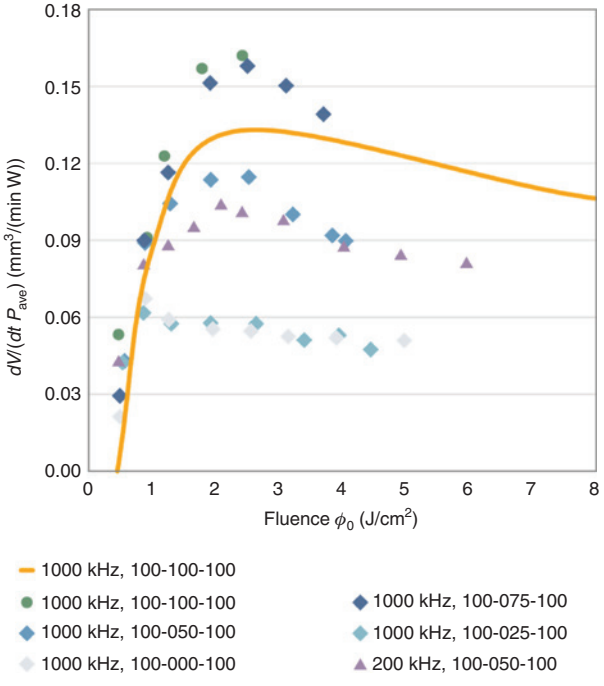

Figure 23: Specific removal rate for the application of a three-pulse burst varying the height of the center pulse on copper (C12 200) [97, 98].

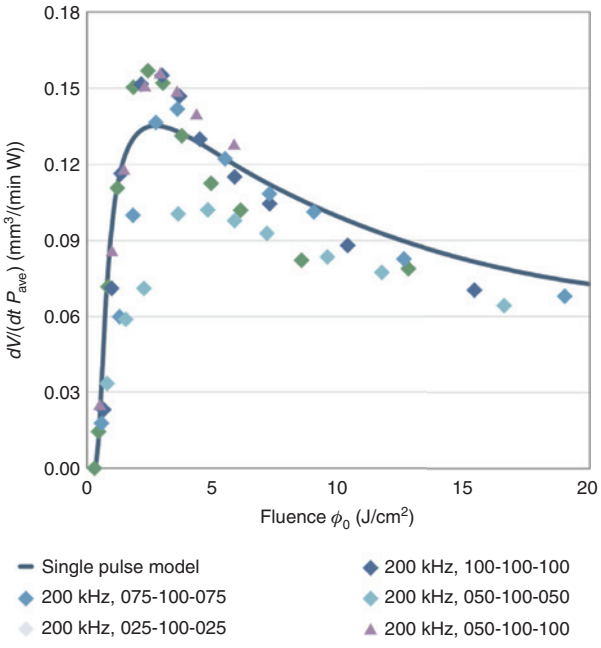

Figure 24: Specific removal rate for the application of a three-pulse burst varying the height of the outer pulses on copper (C12 200) [97, 98].

at the same repetition rate and for the same scanning speed but with the average power doubled. It has the same effect as doubling the repetition rate and the average power for a single pulse. The advantages are twofold: first, the scanning speed, which in some cases may be the limiting factor, does not increase. Second, the number of repetitions or layers can be halved, which means that the production takes only half the time. Just as a side note: Increasing the scanning speed means increasing the acceleration and deceleration time as well, and this, in turn, reduces the duty cycle, the ratio of effective production time on the total production time.

For most materials, the specific removal rate for a single pulse at the optimum point cannot be exceeded. Increasing the repetition rate and average power when keeping the optimum peak fluence, therefore, will result in the highest ablation rate. But even if the ablation efficiency drops slightly, the sum of the ablation rate of two pulses in a burst may exceed that of a single pulse at the same repetition rate. By doing this, the applied average power can be doubled, while repetition rate and scanning speed can be kept. As no other geometrical parameter like the spot size is modified, no further adjustments have to be made.

However, for some materials, this statement is only partially true. Figure 22 shows the specific removal rate for copper (C12 200) as a function of the peak fluence for different pulse burst configurations at a fixed inter-pulse distance of 12 ns. In contrast to steel, the maximum specific removal rate for a single pulse can be exceeded by approximately 15% by applying a three-pulse burst or a five-pulse burst, whereas it drops drastically for a two-pulse burst. The application of a three-pulse burst, thus tripling the average power at the same fixed repetition rate, will raise the ablated volume per time by a factor of $1.15 \times 3 = 3.45$, and the productivity can be increased by the same factor. This rise cannot be achieved by only tripling the repetition rate. In addition, reducing the height of the center pulse to 75% of the height of the first and the last pulse does not reduce the specific removal rate, and reducing the height of the outer pulses to 50% of the height of the center pulse retains the specific removal rate on the level of a single pulse.

As shown in Figures 23 and 24, when applying this three-pulse burst configuration, 50%–100%–50%, i.e. the total pulse energy is doubled, and the ablation rate can be

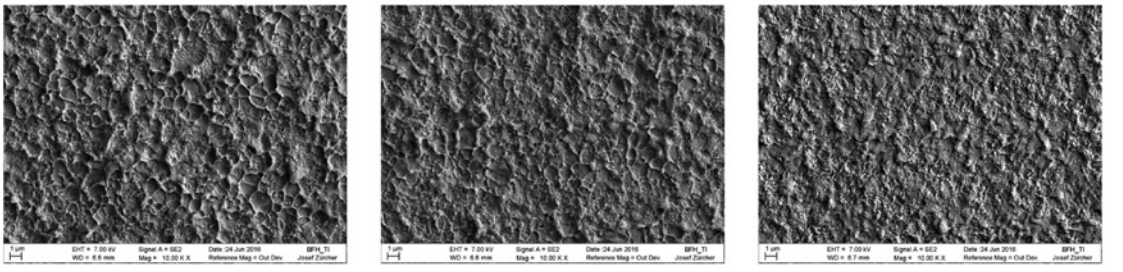

1000 kHz	1000 kHz	1000 kHz
64 Layers	64 Layers	64 Layers
100-100-100	100-050-100	100-000-100
0.162 mm³/(min W)	0.114 mm³/(min W)	0.054 mm³/(min W)

Figure 25: SEM images of machined copper surfaces according to Figure 23 and Figure 24; approximate optimum peak fluence $\phi_{0,opt} = 2.6$ J/cm².

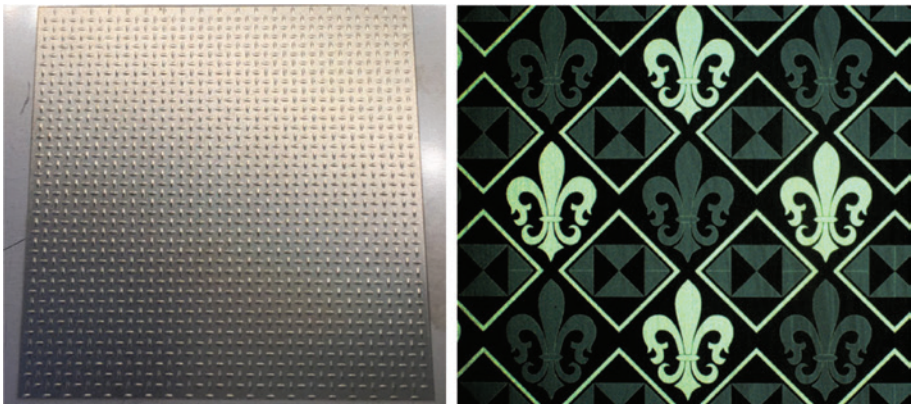

Figure 26: Examples of microstructuring/surface modification and polishing with ultra-short laser pulses on stainless steel AISI 304.

Figure 27: Examples of microstructuring/surface modification and polishing with ultra-short laser pulses on stainless steel AISI 304.

tripled at the same repetition rate. Figure 25 shows SEM images of the surface machined with different configurations of pulse bursts.

This feature can be applied as long as the machining quality still fulfills the requirements. Taking into account the findings of Weber et al., the utilization of the pulse bursts can be used to intentionally generate a molten layer on the surface of the workpiece. Figures 26 and 27 show examples of surface modifications and polishing.

Melting of the surface is used to polish metal parts, and to a certain degree, this works for ultra-fast lasers as well. Although the application of a cost-intense laser, designed for 'cold ablation' appears weird on the first glimpse, it might become economic on the second view in a two-step combination with the ablation process.

Furthermore, the generation of a molten layer for microstructuring applications can directly increase the ablation efficiency. In general, the ablation of molten material is a thermal process and likely more efficient; the ablation efficiency rises drastically for microsecond pulses.

The appearance of holes and bumps on the surface during micromachining by ultra-fast laser radiation is not only a question of quality but, for a few materials, a question of efficiency as well. The rough surface decreases the amount of energy for the ablation process, and at a certain degree of surface roughness, the ablation process stops completely. If the appearance of holes and bumps can be avoided by melting a thin layer on the surface, such that the emerging holes and bumps are leveled out, the ablation efficiency can be kept high [99, 100].

References

[1] New York Times: W. M. Freeman; May 6, 1964, "Theodore H. Maiman, Developer of the Laser Calls It 'A Solution Seeking a Problem'".
[2] L. E. Hargrove, R. L. Fork and M. A. Pollack, Appl. Phys. Lett. 5:1, 4–5 (1964).
[3] H. W. Mocker and R. J. Collins, Appl. Phys. Lett. 7, 270 (1965).

[4] F. X. Kärtner, E. P. Ippen and S. T. Cundiff, in: 'Femtosecond Optical Frequency Comb: Principle, Operation, and Applications', Ed. by J. Ye and S. T. Cundiff (Springer, Boston, MA, 2005).
[5] U. Keller, in: 'Landolt-Börnstein, Group VIII/1B1, Laser Physics and Applications, Subvolume B: Laser Systems, Part 1', Ed. by G. Herziger, H. Weber, and R. Proprawe (Springer-Verlag, Berlin, Heidelberg, New York, October 2007), pp. 33–167, ISBN 978-3-540-26033–26032.
[6] U. Keller, Appl. Phys. B 58, 347–363 (1994).
[7] D. Strickland and G. Mourou, Opt. Commun. 56, 219 (1985).
[8] Trumpf Laser GmbH, https://www.trumpf.com/de_INT/produkte/laser/kurz-und-ultrakurzpulslaser/.
[9] Edgwave GmbH, http://www.edge-wave.de/web/produkte/ultra-short-pulse-systeme/.
[10] Amphos GmbH, http://www.edge-wave.de/web/produkte/ultra-short-pulse-systeme/.
[11] Fraunhofer-Institut für LasertechnikILT, Aachen, https://www.ilt.fraunhofer.de/de/technologiefelder/laser-und-optik/ultrakurzpulslaser.html.
[12] Institut für Strahlwerkzeuge (IFSW), Stuttgart, http://www.ifsw.uni-stuttgart.de/produkte/produkte.html.
[13] B. N. Chichkov, C. Momma, S. Nolte, F. von Alvensleben and A. Tünnermann, Appl. Phys. A 63, 109 (1996).
[14] C. Momma, S. Nolte, B. N. Chichkov, F. V. Alvensleben and A Tünnermann, Appl. Surf. Sci. 109–110, 15–19 (1997).
[15] C. Momma, B. N. Chichkov, S. Nolte, F. von Alvensleben, A. Tünnermann, et al., Opt. Commun. 129, 134–142 (1996).
[16] D. Breitling, A. Ruf and F. Dausinger, in: 'Proc. SPIE 5339, Photon Processing in Microelectronics and Photonics III' (15 July 2004).
[17] F. Dausinger, H. Hugel and V. I. Konov, in: 'Proc. SPIE 5147, ALT'02 International Conference on Advanced Laser Technologies', 14 November (2003).
[18] G. Račiukaitis, M. Brikas, P. Gečys, B. Voisiat and M. Gedvilas, JLMN J. Laser Micro/Nanoeng. 4, 186–191 (2009).
[19] B. Neuenschwander, G. F. Bucher, C. Nussbaum, B. Joss, M. Muralt, et al., in: 'Proc. SPIE 7584, Laser Applications in Microelectronic and Optoelectronic Manufacturing (LAMOM) XV', 75840R, 18 February (2010).
[20] B. Neuenschwander, B. Jaeggi, M. Schmid, V. Rouffiange and P.-E. Martin, in: 'Proc. SPIE 8243, Laser Applications in Microelectronic and Optoelectronic Manufacturing (LAMOM) XVII', 824307, 16 February (2012). doi: 10.1117/12.908583.
[21] B. Lauer, B. Jäggi and B. Neuenschwander, Phys. Procedia 56, 963–972 (2014).
[22] B. Jaeggi, B. Neuenschwander, S. Remund and T. Kramer, in: 'Proc. SPIE 10091, Laser Applications in Microelectronic and Optoelectronic Manufacturing (LAMOM) XXII', 100910J, 20 February (2017). doi: 10.1117/12.2253696.
[23] B. Jaeggi, S. Remund, R. Streubel, B. Goekce, S. Barcikowski, et al., JLMN J. Laser Micro/Nanoeng. 12, 258–266 (2017).
[24] S. Nolte, C. Momma, H. Jacobs, A. Tünnermann, B. N. Chichkov, et al., J. Opt. Soc. Am. B 14, 2716–2722 (1997).
[25] K.-H. Leitz, B. Redlingshöfer, Y. Reg, A. Otto and M. Schmidt, Phys. Procedia 12(Part B), 230–238 (2011).
[26] S. I. Anisimov, A. M. Bonch-Bruevich, M. A. El'yashevich, Y. A. Imas, N. A. Pavlenko, et al., Sov. Phys. Tech. Phys. 11, 945–952 (1967).
[27] S. I. Anisimov, B. L. Kapeliovich and T. L. Perel'man, Sov. Phys.-JETP 39, 375–377 (1974).
[28] B. Rethfeld, D. S. Ivanov, M. E Garcia and S. I. Anisimov, J. Phys. D: Appl. Phys. 50, 193001 (2017).
[29] D. S. Ivanov and L. V. Zhigilei, Phys. Rev. B 68, 064114 (2003).
[30] B. N. Chichkov, C. Momma, S. Nolte, F. von Alvensleben, and A. Tünnermann, Appl. Phys. A 63, 109–115 (1996).
[31] C. Wu and L.V. Zhigilei, Appl. Phys. A 114, 11 (2014).
[32] C. F. Richardson and P. Clancy, Mol. Sim. 7, 335 (1991).
[33] X. Wang and X. Xu, J. Heat Transfer 124, 265 (2002).
[34] D. S. Ivanov and L. V. Zhigilei, Phys. Rev. B 68, 064114 (2003).
[35] D. S. Ivanov and L.V. Zhigilei, Phys. Rev. Lett. 91, 105701 (2003).
[36] Z. Lin and L.V. Zhigilei, Phys. Rev. B 73, 184113 (2006).
[37] L. V. Zhigilei, Z. Lin and D.S. Ivanov, J. Phys. Chem. C 113, 11892 (2009).
[38] Z. Lin, E. M. Bringa, E. Leveugle and L. V. Zhigilei, J. Phys. Chem. C 114, 5686 (2010).
[39] E. T. Karim, Z. Lin and L. V. Zhigilei, AIP Conf. Proc. 1464, 280 (2012).
[40] Z. Lin, R. A. Johnson and L. V. Zhigilei, Phys. Rev. B 77, 214108 (2008).
[41] D. S. Ivanov, Z. Lin, B. Rethfeld, G. M. O'Connor, T. J. Glynn, et al., J. Appl. Phys. 107, 013519 (2010).
[42] C. Wu, D. A. Thomas, Z. Lin and L. V. Zhigilei, Appl. Phys. A 104, 781 (2011).
[43] L. V. Zhigilei and B. J. Garrison, J. Appl. Phys. 88, 1281 (2000).
[44] S. I. Anisimov, V. V. Zhakhovskii, N. A. Inogamov, K. Nishihara, A. M. Oparin, et al., JETP Lett. 77, 606 (2003).
[45] E. Leveugle, D. S. Ivanov and L. V. Zhigilei, Appl. Phys. A 79, 1643 (2004).
[46] L. V. Zhigilei, D. S. Ivanov, E. Leveugle, B. Sadigh, E. M. Bringa, Proc. SPIE 5448, 505 (2004).
[47] A. K. Upadhyay and H. M. Urbassek, J. Phys. D Appl. Phys. 38, 2933 (2005).
[48] A. K. Upadhyay, N. A. Inogamov, B. Rethfeld and H. M. Urbassek, Phys. Rev. B 78, 045437 (2008).
[49] B. J. Demaske, V. V. Zhakhovsky, N. A. Inogamov and I. I. Oleynik, Phys. Rev. B 82, 064113 (2010).
[50] S. I. Ashitkov, N. A. Inogamov, V. V. Zhakhovskii, Y. N. Emirov, M. B. Agranat, et al., JETP Lett. 95, 176 (2012).
[51] E. Ohmura and I. Fukumoto, Int. J. Jpn. Soc. Prec. Eng. 30, 128 (1996).
[52] L. V. Zhigilei, P. B. S. Kodali and B. J. Garrison, J. Phys. Chem. B 101, 2028 (1997).
[53] R. F. W. Herrmann, J. Gerlach and E. E. B. Campbell, Appl. Phys. A 66, 35 (1998).
[54] X. Wu, M. Sadeghi and A. Vertes, J. Phys. Chem. B 102, 4770 (1998).
[55] C. Schäfer, H. M. Urbassek and L. V. Zhigilei, Phys. Rev. B 66, 115404 (2002).
[56] L. V. Zhigilei, Appl. Phys. A 76, 339 (2003).
[57] L. V. Zhigilei, E. Leveugle, B. J. Garrison, Y. G. Yingling and M. I. Zeifman, Chem. Rev. 103, 321 (2003).
[58] P. Lorazo, L. J. Lewis and M. Meunier, Phys. Rev. Lett. 91, 225502 (2003).
[59] N. N. Nedialkov, P. A. Atanasov, S. E. Imamova, A. Ruf, P. Berger, et al., Appl. Phys. A 79, 1121 (2004).
[60] C. Cheng and X. Xu, Phys. Rev. B 72, 165415 (2005).
[61] P. Lorazo, L. J. Lewis and M. Meunier, Phys. Rev. B 73, 134108 (2006).

[62] S. Amoruso, R. Bruzzese, X. Wang, N. N. Nedialkov and P. A. Atanasov, J. Phys. D Appl. Phys. 40, 331–340 (2007).
[63] M. B. Agranat, S. I. Anisimov, S. I. Ashitkov, V. V. Zhakhovskii, N. A. Inogamov, et al., Appl. Surf. Sci. 253, 6276 (2007).
[64] E. Leveugle and L. V. Zhigilei, J. Appl. Phys. 102, 074914 (2007).
[65] M. Prasad, P. Conforti and B. J. Garrison, J. Appl. Phys. 101, 103113 (2007).
[66] L. Zhang and X. Wang, Appl. Surf. Sci. 255, 3097 (2008).
[67] M. Gill-Comeau and L. J. Lewis, Phys. Rev. B 84, 224110 (2011).
[68] L. V. Zhigilei, A. N. Volkov, E. Leveugle and M. Tabetah, Appl. Phys. A 105, 529 (2011).
[69] S. Sonntag, C. T. Paredes, J. Roth and H.-R. Trebin, Appl. Phys. A 104, 559 (2011).
[70] G. Norman, S. Starikov, V. Stegailov, V. Fortov, I. Skobelev, et al., J. Appl. Phys. 112, 013104 (2012).
[71] X. Li and L. Jiang, Appl. Phys. A 109, 367 (2012).
[72] M. Shugaev, C. Wu, O. Armbruster, A. Naghilou, N. Brouwer, et al., MRS Bull. 41, 960–968 (2016).
[73] C.-J. Lin, F. Spaepen and D. Turnbull, J. Non Cryst. Solids 61–62, 767 (1984).
[74] C. Wu, M. S. Christensen, J.-M. Savolainen, P. Balling and L. V. Zhigilei, Phys. Rev. B Condens. Matter 91, 035413 (2015).
[75] C. Wu and L. V. Zhigilei, J. Phys. Chem. C 120, 4438 (2016).
[76] X. Sedao, M. V. Shugaev, C. Wu, T. Douillard, C. Esnouf, et al., ACS Nano 10, 6995 (2016).
[77] J. A. Alonso and J. M. Lopez, Mater. Lett. 4, 316 (1986).
[78] J. Finger and M. Reininghaus, Opt. Express 22, 18790–18799 (2014).
[79] R. Weber, T. Graf, P. Berger, V. Onuseit, M. Wiedenmann, et al., Opt. Express 22, 11312–11324 (2014).
[80] R. Weber, T. Graf, C. Freitag, A. Feuer, T. Kononenko, et al., Opt. Express 25, 3966–3979 (2017).
[81] F. Bauer, A. Michalowski, T. Kiedrowski and S. Nolte, Opt. Express 23, 1035–1043 (2015).
[82] J. König, S. Nolte and A. Tünnermann, Opt. Express 13, 10597–10607 (2005).
[83] H. Schlueter, B. Jaeggi, B. Neuenschwander and M. Zimmermann, Laser Focus World 52, 41–44 (2016).
[84] S. Russ, R. Gebs, L. Bauer, U. Keller, T. Meyer et al., Paper 161, Lasers in Manufacturing 2015 (2015).
[85] J. Lopez, R. Kling, R. Torres, A. Lidolff, M. Delaigue, et al., Proc. SPIE 8243, (2012).
[86] F. Di Niso, C. Gaudiuso, T. Sibillano, F. P. Mezzapesa, A. Ancona, et al., Phys. Procedia 41, 698–707 (2013).
[87] J. Lopez, A. Lidolff, M. Delaigue, C. Hönninger, S. Ricaud, et al., Paper M401, ICALEO 2011, (2011).
[88] R. Le Harzig, D. Breitling, M. Weikert, S. Sommer, C. Föhl, et al., Appl. Surf. Sci. 249, 322–331 (2005).
[89] B. Sallé, O. Gobert, P. Meynadier, M. Perdrix, G. Petite, et al., Appl. Phys. A 69, 381–383 (1999).
[90] Pulsar Photonics GmbH, https://www.pulsar-photonics.de/systemtechnik/.
[91] Hamamatsu Photonics K.K., http://www.hamamatsu.com/jp/en/4015.html.
[92] Holoeye Photonics AG, https://holoeye.com/spatial-light-modulators/.
[93] C. Hartmann, T. Fehr, M. Brajdic and A. Gillner, JLMN J. Laser Micro Nanoeng. 2, 44–48 (2007).
[94] C. Hartmann and A. Gillner, in: 'ICALEO Congress Proceedings - Laser Microprocessing Conference', Orlando (2007), 38–44.
[95] R. Knappe, H. Haloui, A. Seifert, A. Weis and A. Nebel, in: 'Proc. SPIE 7585, Laser-based Micro- and Nanopackaging and Assembly IV', 75850H, 23 February (2010). doi.org/10.1117/12.842318.
[96] C. Emmelmann and J. P. Calderón Urbina, Phys. Procedia 12(B), 172–181 (2011).
[97] T. Kramer, Y. Zhang, S. Remund, B. Jaeggi, A. Michalowski, et al., JLMN J. Laser Micro Nanoeng. 12, 267–273 (2017).
[98] T. Kramer, B. Neuenschwander, B. Jäggi, S. Remund, et al., Phys. Procedia 83, 123–134 (2016).
[99] M. Sailer, F. Bauer, J. Kleiner and M. Kaiser, in: 'Lasers in Manufacturing Conference (2015)'.
[100] B. Jaeggi, S. Remund, Y. Zhang, T. Kramer and B. Neuenschwander, JLMN J. Laser Micro Nanoeng. 12, 107–114 (2017).